RSC Advances

PAPER

View Article Online
View Journal | View Issue



Cite this: *RSC Adv.*, 2026, **16**, 12246

# Mechanistic insights into $CO_2$-driven hydration of propargylic alcohols catalyzed by oxometallate ionic liquids

Neveen I. Atallah,[ab] Mohamed E. El-Khouly, *[a] Ahmed Abdelmoneim,[a] Kei Ohkubo [c] and Morad M. El-Hendawy*[de]

Oxometallate-based ionic liquids, exemplified by tetrabutylammonium molybdate, have recently emerged as efficient and recyclable catalysts for $CO_2$-assisted hydration of propargylic alcohols under mild conditions. In this work, density functional theory (DFT) is employed to provide an in-depth mechanistic investigation of the catalytic role of oxomolybdate-based ionic liquids in the formation of α-hydroxy ketones. The catalytic transformation proceeds through two interconnected cycles involving seven elementary steps, in which bifunctional activation by $MoO_4^{2-}$–$CO_2$ adducts integrates $CO_2$ capture and activation with substrate transformation. Hydrolysis of the cyclic carbonate intermediate is identified as the overall rate-determining step, with a computed free energy barrier of 28.7 kcal $mol^{-1}$. A comparative analysis using the oxochromate analogue reveals comparable overall barriers but distinct rate-limiting steps, highlighting the influence of the metal center on individual reaction energetics. Electron Localization Function (ELF) and Non-Covalent Interaction (NCI) analyses elucidate the electronic reorganization and intermolecular interactions governing these differences. These insights establish a theoretical framework for the rational design of advanced oxometallate catalysts for efficient $CO_2$ utilization.

Received 29th January 2026
Accepted 24th February 2026

DOI: 10.1039/d6ra00803h

rsc.li/rsc-advances



## 1. Introduction

The rising concentration of atmospheric carbon dioxide ($CO_2$) has become a significant environmental challenge, prompting extensive research into its utilization as a renewable $C_1$ feedstock.[1] Beyond its established role as a reagent in carboxylation reactions, $CO_2$ is increasingly being employed as a temporary catalyst or promoter in chemical transformations. In such systems, the catalyst activates $CO_2$, which in turn promotes substrates to generate key intermediates without being permanently incorporated into the final product, thereby enabling new reaction pathways under mild conditions. A well-known example is the $CO_2$-promoted hydration of propargylic alcohols to afford valuable α-hydroxy ketones, typically proceeding *via* the initial formation of a cyclic carbonate intermediate.[2–4]

α-Hydroxy ketones constitute important structural motifs widely found in natural products and serve as versatile precursors for the synthesis of diverse functional molecules.[5] The hydration of propargylic alcohols represents a particularly attractive route to α-hydroxy ketones due to its perfect atom economy and the broad availability of starting materials. Nevertheless, traditional hydration methods often require harsh acidic conditions,[6] utilizing reagents such as $H_2SO_4$ or rare transition-metal salts including Au,[7,8] Ag,[9] and Ru,[10] which may induce undesirable side reactions. To overcome these limitations, $CO_2$-promoted indirect hydration has emerged as a promising alternative. This method first converts propargylic alcohols and $CO_2$ into α-alkylidene cyclic carbonates, which subsequently undergo *in situ* hydrolysis to yield the desired α-hydroxy ketones Fig. 1. Notably, the basic reaction conditions employed in this approach suppress the Meyer–Schuster rearrangement,[11] while the overall process remains significantly milder than direct hydration, making it an attractive route for sustainable synthesis. Simultaneously with experimental initiatives, computational chemistry, specifically the DFT method, has emerged as a crucial instrument for clarifying the complex mechanisms of $CO_2$-promoted reactions. Significant atomic-level insights that are frequently unavailable through

[a]*Nano Science Program, Faculty of Basic and Applied Science, Egypt-Japan University of Science and Technology, New Borg El-Arab City, Alexandria, Egypt. E-mail: mohamed.elkhouly@ejust.edu.eg*

[b]*Nano Science Program, Institute of Nanoscience and Nanotechnology, Kafrelsheikh University, Egypt*

[c]*Institute for Open and Transdisciplinary Research Initiatives (OTRI), The University of Osaka, 1-6 Yamada-oka, Suita 565-0871, Osaka, Japan*

[d]*Molecular Science Institute, School of Chemistry, University of the Witwatersrand, Private Bag X3, Johannesburg, 2050, South Africa. E-mail: morad.el-hendawy@wits.ac.za*

[e]*Department of Chemistry, Faculty of Science, New Valley University, Kharga 72511, Egypt*

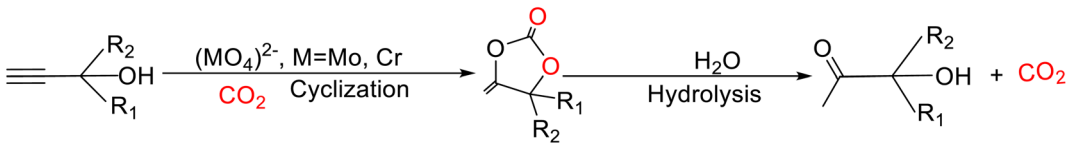


Fig. 1 The $CO_2$-assisted catalytic hydration of propargylic alcohols to form α-hydroxy ketones.

experimentation alone have been obtained through theoretical investigations. There are several DFT studies that explored the mechanistic pathway for anionic liquids. For instance, DFT calculations in a study on the heterogeneous ZnO/ionic liquid-catalyzed hydration of propargylic alcohols showed the exact synergistic roles of the catalyst components and determined that the rate-determining step was the hydrolysis of the cyclic carbonate intermediate.[12] Despite this, the full DFT mechanistic pathway for homogenous, transition-metal–oxygen anions such as oxometallate-ionic liquids (OM-ILs) that function by a unique anionic activation method *via* a $CO_2$ adduct is still unknown. Beyond this particular reaction, DFT has been used extensively to comprehend how various catalysts activate $CO_2$. Research on organocatalysts, such as guanidines and N-heterocyclic carbenes (NHCs), has quantified the nucleophilicity and function of catalyst-$CO_2$ adducts by computing their production and reactivity.[13]

Current efforts in this field have focused largely on homogeneous catalysts, including metal complexes,[14] metal halides,[15] organic bases,[16] and ionic liquids (ILs),[17,18] owing to their high reactivity under mild conditions. Among these, IL-based catalytic systems have gained substantial attention due to their exceptional chemical and thermal stability, tunable structures, and recyclability.[19,20] Of particular interest in recent years are oxometallate-based ionic liquids (OM-ILs), in which the catalytically active anion contains a high-valent transition metal. The remarkable redox behavior, structural diversity, and oxygen-rich nature of oxometallates—including tungsten-, molybdenum- and vanadium-based species—contribute to their strong nucleophilicity and ability to activate $CO_2$ *via* adduct formation.[21–25]

Recently, Wang *et al.* studied the oxometallate-based ionic liquid, tetrabutylammonium molybdate, which efficiently catalyzes the $CO_2$-promoted hydration of propargylic alcohols to α-hydroxy ketones without additives, representing the first use of such ILs for this reaction.[26] It activates $CO_2$, forming $MoO_4$–$CO_2$ adducts and can be synthesized from ammonium molybdate wastewater, offering a sustainable approach. This system shows promise for industrial $CO_2$ conversion and environmental applications, with future work focused on optimizing performance, expanding substrate scope, and evaluating long-term stability.

This work explores the reaction mechanism of $CO_2$-promoted hydration and to evaluates the catalytic potential of $(MO_4)^{2-}$-based ILs (M = Mo, Cr), focusing on how electronic differences between isoelectronic oxometallate anions influence activity. By combining DFT calculations with NCI and ELF analyses, we elucidate the reaction pathway and key stabilizing interactions.

## 2. Computational details

Geometry optimizations and vibrational frequency analyses were carried out in the gas phase with the M06 density functional[27] including Grimme's empirical dispersion correction[28] with mixed basis sets. In this regard, the 6-31+G (d, p) basis set was employed for non-metal atoms (C, O, H), while LANL2DZ was used for the metal centers (Mo and Cr).[29,30] All transition states were confirmed to connect the corresponding reactants and products and were characterized by a single imaginary frequency. To take into consideration the experimental environment, single-point energy calculations in water were performed on the optimized gas-phase geometries using the same functional with higher-level mixed basis sets: LANL2TZ (f) with f-polarization functions and the Hay–Wadt effective core potential (ECP)[29–31] for Mo and Cr, and 6-311+G (2d, p) for all other atoms to refine the electronic energies. In this context, the SMD solvation model was used to account for the solvent effect.[32] The basic DFT reactivity descriptors and condensed Fukui function for electrophilic attack ($f_k^-$) was also calculated. All DFT computations were performed using Gaussian 16, Revision C.01.[33] Reported relative energies correspond to Gibbs free energies in the singlet state at 298.15 K and 1 atm, expressed in kcal $mol^{-1}$. Chemcraft was used to visualize and analyze the results.[34] On the other hand, the 2D and 3D plots for ELF and NCI were all calculated using Multiwfn 3.8 software.[34,35] Additionally, as implemented in NBO 7.0 program,[36] natural energy decomposition analysis (NEDA) was calculated to determine the electronic interactions in the oxometallate-$CO_2$ adduct. The total interaction energy ($\Delta E_{int}$) can be decomposed to Core repulsion (CORE), charge transfer (CT), and electrical interaction (EL) where the electrical term ($\Delta E_{EL}$) arises from classical electrostatic ($\Delta E_{ES}$) and polarization interactions ($\Delta E_{POL}$+ $\Delta E_{SE}$):[37]

$$\Delta E_{EL} = \Delta E_{ES} + \Delta E_{POL} + \Delta E_{SE} \quad (1)$$

$\Delta E_{CORE}$ is given as follow:

$$\Delta E_{CORE} = \Delta E_{XC} + \Delta E_{DEF} - \Delta E_{SE} \quad (2)$$

Here, $\Delta E_{XC}$ is the exchange–correlation interaction while $\Delta E_{DEF}$ represents the deformation energy.

In this regard, $\Delta E_{int}$ can be given as follow:

$$\Delta E_{int} = \Delta E_{CT} + \Delta E_{DEF} + \Delta E_{XC} + \Delta E_{ES} + \Delta E_{POL} \quad (3)$$

Additionally, the binding energy $\Delta E_b$ is defined as:

$$\Delta E_b = \Delta E_{int} + \Delta E_{DEF} \quad (4)$$

## 3. Results and discussion

Based on the experimental study by Wang *et al.*, a catalytic cycle for oxomolybdate-based ionic liquid catalyzed $CO_2$-assisted hydration of propargylic alcohols for α-hydroxy ketones synthesis was proposed.[26] At the beginning, the effective catalyst—a molybdate–carbonate adduct ($MoO_4$–$CO_2$)—is formed through the nucleophilic attack of $(MoO_4)^{2-}$ on the $CO_2$ species. In this context, the bond angle of free $CO_2$ significantly reduced from 180° to 123° making it in the activated form,[38,39] As known, Cr, Mo, and W are consecutive elements in Group 6 of the periodic table, and their properties vary gradually across the group. The experimental study showed that $WO_4$-based catalysts exhibit lower catalytic performance compared to $MoO_4$-based catalysts. Therefore, we decided to examine the catalytic activity of $CrO_4$-based catalysts due to the crucial role of the metallic center in this catalytic process.

The electron-donating capacity of the studied oxometallic species, before adduct formation with $CO_2$, can be rationalized using the quantum chemical descriptors that based on Hard and Soft Acids and Bases (HSAB) concept, as listed in Table 1.[40] The maximum electronic charge transfer ($\Delta N_{max}$) from the catalyst to $CO_2$ is 1.42 and 1.19 for the oxomolybdate and oxochromate species, respectively. The higher $\Delta N_{max}$ value for the oxomolybdate arises from its higher chemical potential (less negative) and greater softness (more easily polarizable).

Moreover, the condensed Fukui function, which is defined as the sensitivity of the electron density $\rho(r)$ at different points in a particular species to the change in the number of electrons ($N$) in the molecular system at a constant external potential $n(r)$, was calculated to further comprehend the local reactivity.[41] At atomic site $k$, condensed Fukui functions corresponding to electrophilic attack ($f_k^-$) and nucleophilic attack ($f_k^+$) are expressed as follow:[42]

$$f_k^+ = q_k^{(N+1)} - q_k^{(N)} \quad (5)$$

$$f_k^- = q_k^{(N)} - q_k^{(N-1)} \quad (6)$$

where the electron populations at $k$ atoms for a given species' neutral, cationic, and anionic states are denoted by the symbols $q_k^{(N)}$, $q_k^{(N-1)}$, and $q_k^{(N+1)}$, respectively. In this regard, the increase in Fukui function ($f_k^-$) reflects the increase in nucleophilicity of the oxygen atoms of the oxometallic species, which is larger by 8% for the molybdate system.[43]

Table 1 The calculated chemical reactivity descriptors for the $[MoO_4]^{2-}$ and $[CrO_4]^{2-}$ catalysts, including ionization potential (IP), electron affinity (EA), chemical potential ($\mu$), softness ($S$), average condensed Fukui function for electrophilic attack ($f_k^-$) for oxygen atoms, global nucleophilicity index ($N$), and maximum electronic charge transfer ($\Delta N_{max}$). IP, EA, $\mu$, and $N$ are in eV; $f_k^-$ and $\Delta N_{max}$ are dimensionless

| Reactivity descriptors | $[MoO_4]^{2-}$ | $[CrO_4]^{2-}$ |
|---|---|---|
| IP | 15.75 | 16.63 |
| EA | 7.56 | 6.80 |
| $\mu$ | −11.66 | −11.72 |
| $S$ | 0.12 | 0.10 |
| $f_k^-$ | 0.25 | 0.23 |
| $N$ | 0.28 | 0.25 |
| $\Delta N_{max}$ | 1.42 | 1.19 |

Based on the hypothesis of Wang *et al.*, we attempted to examine the feasibility of this pathway using DFT model chemistry.[26] Several potential mechanistic routes were computationally explored. As an alternative, the hydration reaction was facilitated by the bare $[MoO_4]^{2-}$ without the molybdate–carbonate adduct formation, as an oxomolybdate anion. The SI (Fig. S1) describes this 'non-adduct' pathway, which is kinetically unfavorable in mild conditions. Thus, the most energetically favorable mechanism was found to be interconnected cyclic mechanism as described in Fig. 2. In this regard, the calculations showed a significant distance of about 3–4 Å between the ammonium nitrogen atom of the cation and the molybdenum atom of the anion in tetrabutylammonium molybdate ($[N_{4444}]_2[MoO_4]$), the most efficient catalyst in the experimental study. This large distance justifies modeling only the catalytically active molybdate anion $(MoO_4)^{2-}$. At such separation, the bulky cation is unlikely to influence the intrinsic reaction pathway electronically and is expected only to impose steric effects that may alter the overall reaction rate. Focusing on the bare anion, therefore, provides an accurate description of the fundamental mechanistic steps while significantly reducing computational cost.[44,45] The mechanism comprises a two-cycle reaction process, Cycles I and II, as shown in Fig. 2. It involves seven elementary steps: three in Cycle I and four in Cycle II.

### 3.1 Cycle I

Cycle I comprises three steps: OH activation, nucleophilic attack and hydrogen migration. The optimized structures of the key intermediates and transition states in Cycle I are shown in Fig. 3. As mentioned before, the molybdate–carbonate adduct ($MoO_4$–$CO_2$) is the effective catalyst. Accordingly, this adduct activate the hydroxyl group of the substrate *via* a hydrogen bond formation of length 1.71 Å, forming the first intermediate ($Int_I$). This interaction costs 7.8 kcal $mol^{-1}$. The carbonated oxyanion attacks the non-terminal acetylenic carbon atom of $Int_I$ through transition state ($TS_I$) to produce $Int_{II}$. This action proceeds through a well-known indicator of nucleophilic attack mechanisms as the linear alkyne (sp-hybridized, ∼180°) convert into a bent, alkene-like structure ($sp^2$-hybridized, 110°) with a bond length of 1.34 Å. This step consumes relatively small energy, 12.9 kcal $mol^{-1}$, ($Int_I \rightarrow TS_I$), leading to the formation of an intermediate ($Int_{II}$) that undergoes further rearrangement and cyclization. A key transformation involves hydrogen migration from $Int_{II}$ to $TS_{II}$ requires $\Delta G$ of 27.9 kcal $mol^{-1}$. In this event, the hydroxyl hydrogen migrates from $O_{13}$ to the carbonanion center ($C_{10}$) to form a relatively high energy oxyanion species, $Int_{III}$. This could motivate the intramolecular cyclization in cycle II (Fig. 4).

### 3.2 Cycle II

The key DFT structures of cycle II are illustrated in Fig. 5. Cycle II begins by the nucleophilic attack of alkoxide center of $Int_{III}$ on

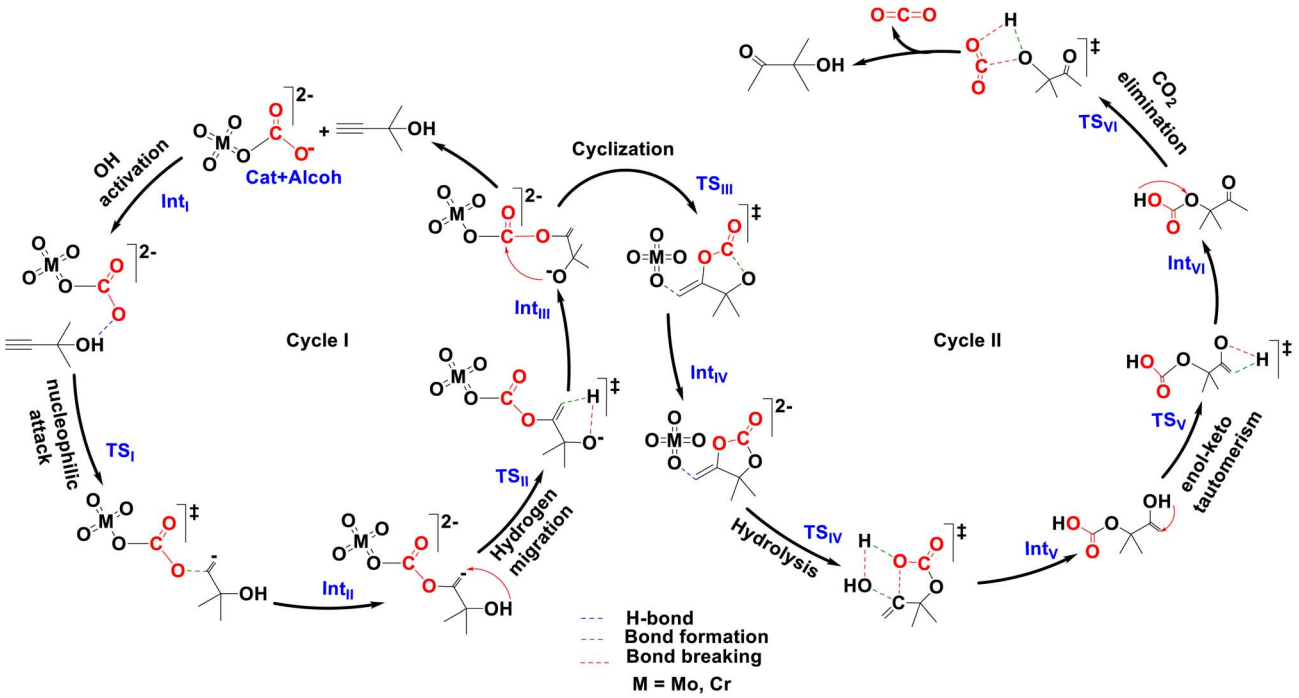


Fig. 2 DFT-validated mechanism of oxometallate-catalyzed $CO_2$-driven hydration to α-hydroxy ketones.

the carbonyl carbon ($C_1$) causing ring closure and formation of a five-membered cyclic carbonate intermediate ($Int_{IV}$) *via* $TS_{III}$. The free energy barrier for this transformation requires 18.0 kcal mol$^{-1}$. $TS_{III}$ of the cyclization is characterized by the formation of a new C–O bond with distance of 1.30 Å.

Following the formation of a five-membered cyclic carbonate, the cycle tends to open through an endrogenic hydrolysis step (0.8 kcal mol$^{-1}$) to form the diol species, $Int_V$. This concerted step includes two bond formation ($C_4$–$O_{10}$ 1.67 Å and $O_3$–$H_{11}$ 1.82 Å) and two bond breaking ($C_4$–$O_3$ 1.84 Å and $O_{10}$–$H_{11}$ 0.99 Å) through four-membered transition state, $TS_{IV}$ (26.9 kcal mol$^{-1}$). The diol species now freed from the molybdenum center. $TS_{IV}$ and $Int_{II}$ are turnover frequency determining transition state (TDTS) and turnover frequency determining intermediate (TDI), respectively, indicating the overall rate determining step with free energy barrier of 29.8 kcal mol$^{-1}$.[46]

The next step, enol-to-keto tautomerism, involves the migration of hydrogen atom ($H_{14}$) from the carbonyl oxygen ($O_{12}$) to the alkenic carbon atom ($C_5$), forming a new bond, $C_5$–$H_{14}$, *via* kite-like four-membered transition state, $TS_V$. According to Hammond's postulate,[47] this transition state is early and closely resembles $Int_V$. This is evidenced by the shorter $O_{12}$–$H_{14}$ bond distance (1.27 Å) compared to the $C_5$–$H_{14}$ bond distance (1.47 Å). Moreover, the transition state is energetically closer to $Int_V$ than to $Int_{VI}$. As anticipated, this process is thermodynamically favored, where the keto species is more stable than the enol one by 14.1 kcal mol$^{-1}$.[48,49]

The last event of this mechanism is the hydrogen shift in the carbonic acid ester group of $Int_{VI}$. In this context, $H_{11}$ atom

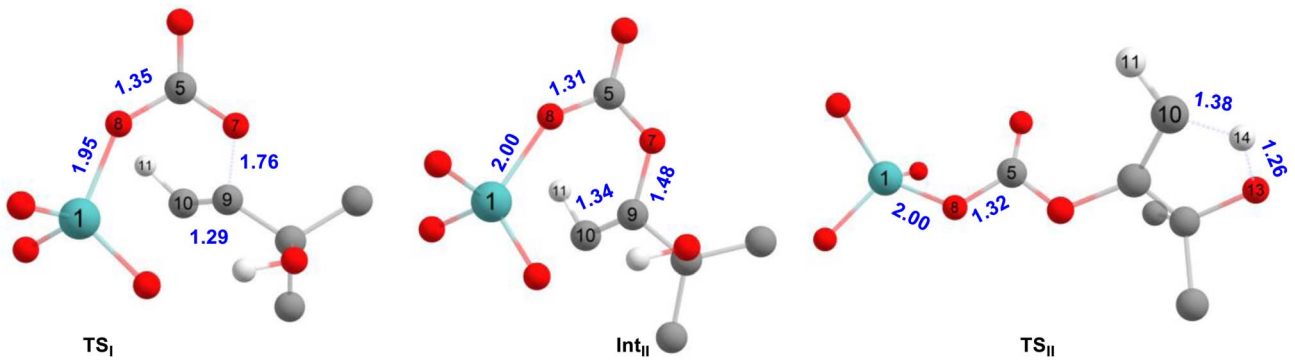


Fig. 3 The optimized structures of the key intermediates and transition states in Cycle I. Dotted lines indicate bond formation, and bond breaking. The key bond lengths are shown in Angstroms (Å). The less relevant H atoms are omitted for clarity.

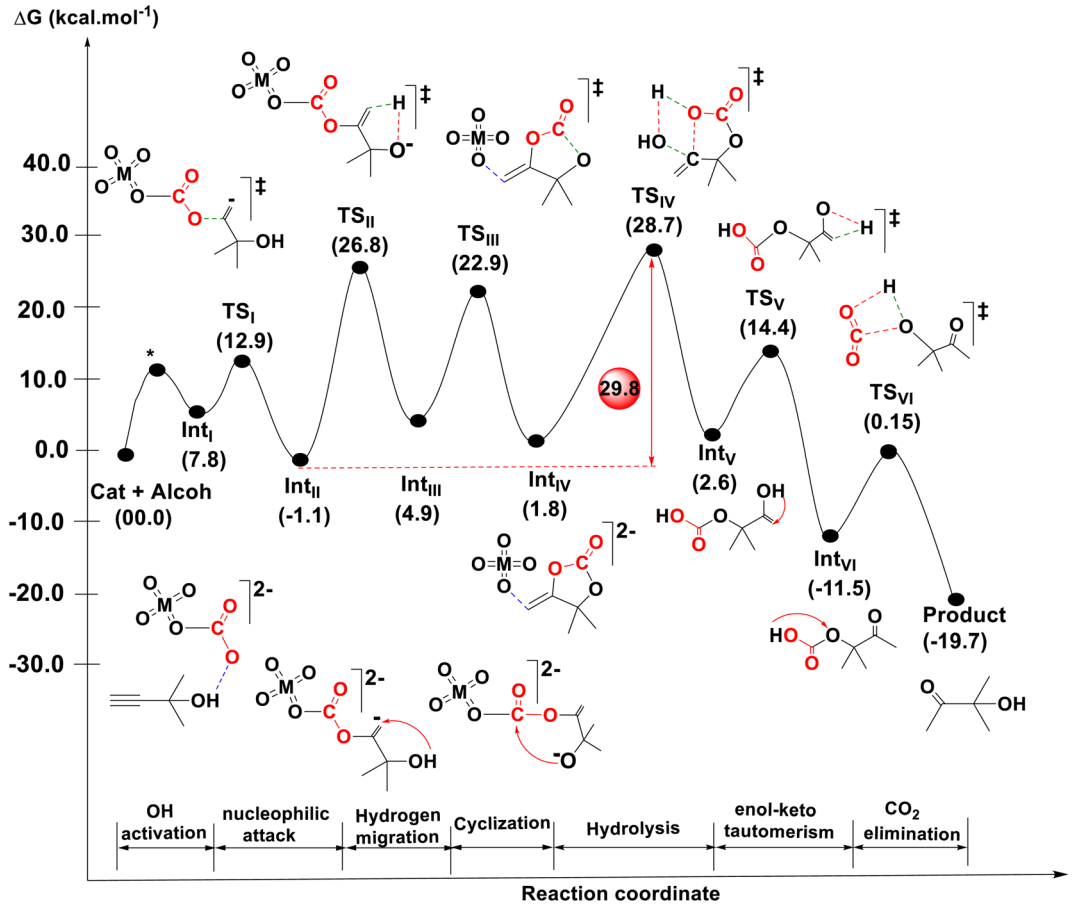


Fig. 4 The free energy profile of oxometallate-catalyzed $CO_2$-driven hydration to α-hydroxy ketones. The sign (*) is an assumed transition state for the barrierless interaction between the catalyst-$CO_2$ adduct and the substrate to form $Int_I$.

transfers from $O_2$ to $O_7$ releasing a $CO_2$ molecule. At this end of the reaction coordinate, product formation takes place. During this concerted step, the $O_7$–$H_{11}$ bond is formed with a length of 1.19 Å, while the $O_2$–$H_{11}$ and $C_1$–$O_7$ bonds are broken, with lengths of 1.29 Å and 1.61 Å, respectively, with a free energy barrier of 11.65 kcal $mol^{-1}$. This in turn has an effect on the bond angle of ($O_2$–$C_1$–$O_3$) where it increased from 124° in $Int_{VI}$ to 145° in $TS_{VI}$ as the system prepares to release the $CO_2$ molecule. The transformation from the propargylic alcohol to the α-hydroxy ketone product is highly exergonic by −19.7 kcal $mol^{-1}$.

### 3.3 Metal center effect on catalytic behavior

In this section, we investigated the metallic center effect on catalytic behavior of the oxometallic species. Fig. 6 depicts the free energy profile of the $CO_2$-driven hydration of propargyl alcohol over $MoO_4$-and $CrO_4$-based catalysts. Both catalysts promote the initial OH activation with a negligible variation in the required energy. The nucleophilic attack step promoted by Mo-based catalyst is energetically favored by 6.9 kcal $mol^{-1}$. Moving to the hydrogen migration step, slightly difference in the energy barrier was observed in both cases. This can be

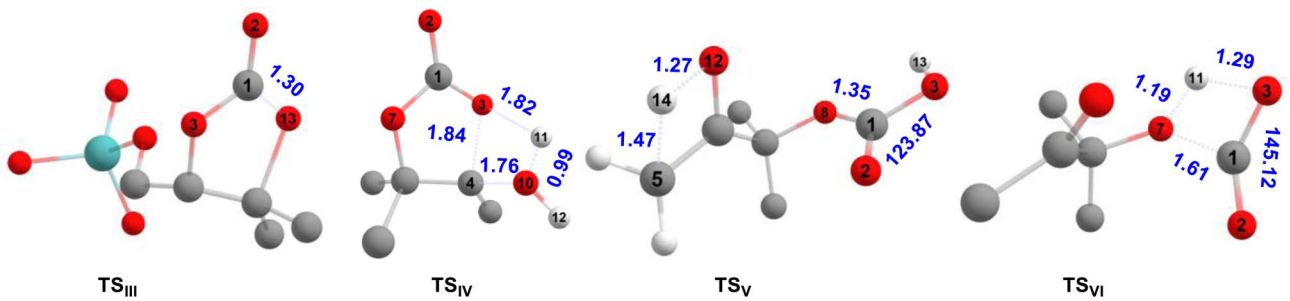


Fig. 5 The optimized structures of the key transition states in Cycle II. Dotted lines indicate bond formation, and bond breaking. The key bond lengths are shown in Angstroms (Å) and angles in degree. The less relevant H atoms are omitted for clarity.

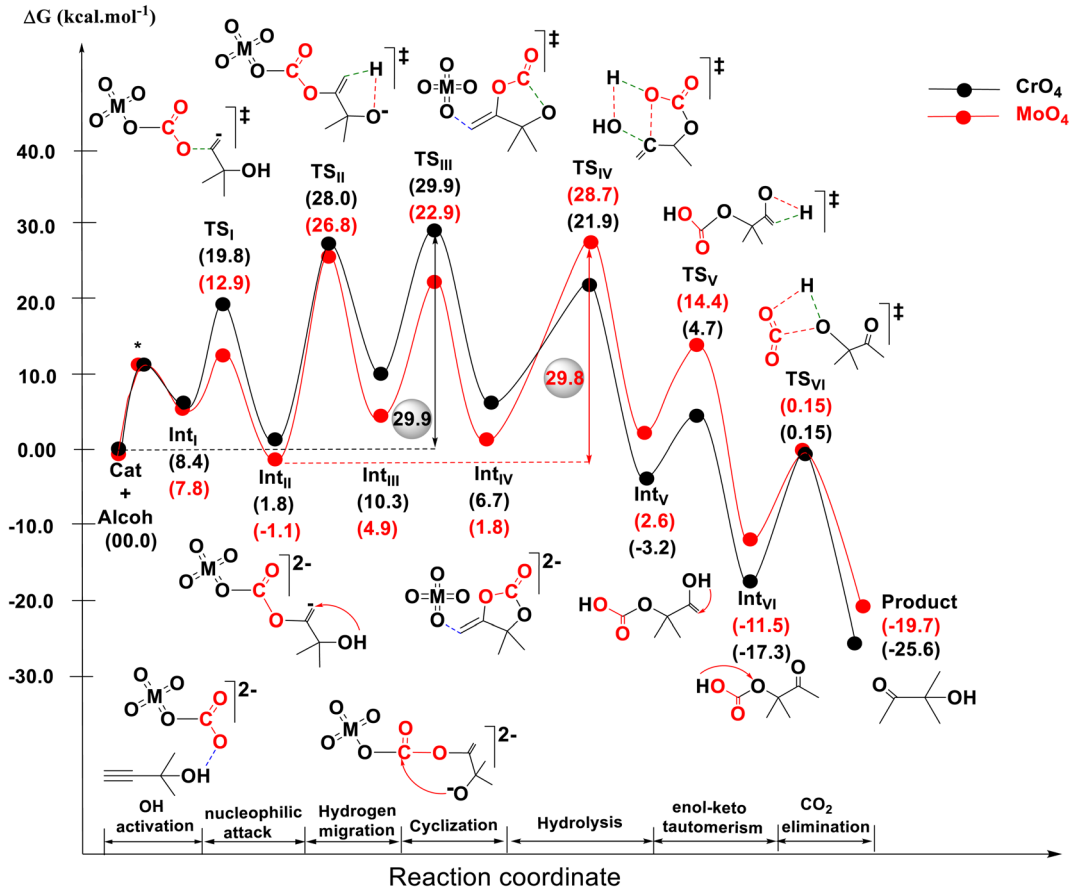


Fig. 6 The free energy profiles of the catalytic reaction using the molybdate and chromate-based catalysts. The sign (*) is an assumed transition state for the barrierless interaction between the catalyst-$CO_2$ adduct and the substrate to form $Int_I$.

attributed to the close energies of $Int_{II}$ and $TS_{II}$. In addition, the catalytic activity of the oxomolybdate species in the nucleophilic attack step is relatively superior. This step is again more favorable than the intramolecular cyclisation step in $Int_{III}$ by $\Delta\Delta G = 7.0$ kcal mol$^{-1}$ when compared to the oxochromate species, as the former more effectively stabilizes the $Int_{III}$ and $TS_{III}$ species.

These kinetic differences arising from the metal centers can be explained by the higher softness of the oxomolybdate anion ($S = 0.12$ eV) compared to oxochromate ($S = 0.10$ eV), as shown in Table 1. The increased softness corresponds to a longer Mo–O bond distance (2.09 Å) relative to Cr–O (1.79 Å). To further understand the electronic basis for this favorability, natural energy decomposition analysis (NEDA) was performed on the active adduct, Table 2. The analysis shows that the $(MoO_4–CO_2)^{2-}$ adduct is more stable, with a total interaction energy ($\Delta E_{int}$) of −144.23 kcal mol$^{-1}$, compared to −102.61 kcal mol$^{-1}$ for the oxochromate adduct. This stability is further supported by significant charge transfer ($\Delta E_{CT}$) values of −663.9 and −462.6 kcal mol$^{-1}$ for the Mo and Cr adducts, respectively.[45]

Table 2 A comparison of natural energy components in (kcal mol$^{-1}$) for the ($MoO_4–CO_2$) and ($MoO_4–CO_2$) using NEDA analysis on NBO7.0 software

| Catalyst | $\Delta E_{DEF}$ | $\Delta E_{ES}$ | $\Delta E_{POL}$ | $\Delta E_{CT}$ | $\Delta E_{int}$ | $\Delta E_b$ |
|---|---|---|---|---|---|---|
| ($MoO_4–CO_2$) | 864.38 | −303.53 | 2.66 | −663.91 | −144.23 | 720.15 |
| ($CrO_4–CO_2$) | 618.44 | −197.34 | −30.08 | −462.63 | −102.61 | 515.83 |

Although geometric distortion of the substrate incurs a high energetic cost ($\Delta E_{DEF} = 864.4$ kcal mol$^{-1}$), the softer Mo center effectively overcomes this penalty, activating the substrate into a more reactive bent conformation by enabling superior orbital overlap and enhanced electron donation into the $CO_2$ $\pi^*$ orbitals ($\Delta E_{CT} = -663.9$ kcal mol$^{-1}$). In contrast, the chromate system relies more on polarization ($\Delta E_{POL} = -30.08$ kcal mol$^{-1}$) and exhibits less electrostatic stabilization ($\Delta E_{ES} = -197.34$ kcal mol$^{-1}$), resulting in a stiffer, less reactive adduct. These results demonstrate that the softer Mo core promotes stronger electron donation into $CO_2$, facilitating efficient activation in Cycle I.[44]

On the other hand, the oxochromate species exhibited higher catalytic activity toward the hydrolysis and enol-to-keto tautomerism steps by $\Delta\Delta G = 6.8$ and 9.7 kcal mol$^{-1}$, respectively. The oxomolybdate species exhibits higher reactivity in the $CO_2$ elimination step, leading to the formation of a more stable product. This kinetic preference arises primarily from the stabilization of $Int_{VI}$ by $\Delta\Delta G = 5.8$ kcal mol$^{-1}$, while the $TS_{VI}$ energy is very comparable to that of the oxochromate species.

Based on the above discussion, although both catalytic systems follow the same catalytic cycle, the TDI and TDTS species differ between them. For the Mo-based cycle, the TDI and TDTS are $Int_{II}$ and $TS_{IV}$, respectively, whereas for the Cr-based cycle, they correspond to the reactants/catalyst system and $TS_{II}$. Despite having comparable overall energy barriers of 29.8 and 29.9 kcal $mol^{-1}$ for the Mo- and Cr-based catalysts, respectively, catalytic performance is not the sole consideration. Factors such as catalyst stability and toxicity are also crucial. Accordingly, the oxomolybdate species is more stable and less toxic than the oxochromate species, the latter being less stable due to the inherent instability of chromium in the +6 oxidation state.[50–52]

### 3.4 Non covalent interactions analysis

Electron Localization Function (ELF) analysis was carried out for the key transition states $TS_I$, $TS_{II}$, $TS_{IV}$, and $TS_V$ to obtain a better understanding of the electronic reorganisations underlying the critical stages of the molybdate-based catalytic cycle, as illustrated in Fig. 7.[53] The ELF isosurface and contour plot for Cycle I displays the electronic reorganization during the initial activation and nucleophilic attack phases. $TS_I$ representing the initial interaction between one of the carbonate oxygen atoms $O_7$, and the nonterminal acetylenic carbon atom $C_9$ of the activated propargylic alcohol, reveal the onset of bond formation and indicate the electrophilic activation of carboxylate group and the increased nucleophilicity of the oxygen atom. The corresponding contour plot suggests an elongated basin of electron localization between $O_7$ and $C_9$, which is indication of a partial bond formation. In the contour plot for $TS_{II}$, which provides hydrogen migration, the migrating hydrogen is positioned between the donor $O_{13}$ and acceptor $C_{10}$, consistent with the bond lengths 1.26 Å ($O_{13}$–$H_{14}$) and 1.38 Å ($H_{14}$–$C_{10}$) observed in Fig. 3. This bridging electron localization signifies that the hydrogen is in an 'in-transit' state, simultaneously weakening its bond with the $O_7$ and forming a new bond with the $C_{10}$. This is confirmed by Hammond's postulate for the endergonic phase which states that the transition state structure approaches the succeeding intermediate more than the reactant.[47]

In Cycle II, the ELF displays the critical RDS hydrolysis and tautomerism steps. The ring-opening step for the rate-determining step $TS_{IV}$ is depicted by the electron localization between $C_4$ and $O_3$ is obviously disrupted (elongated and diffused basin in the counter plot between C and O that are not circled together) at the same time that a new covalent interaction between the water oxygen $O_{10}$ and the carbonyl carbon $C_4$ at a distance of 1.67 Å is formed, see optimized $TS_{IV}$ in Fig. 5 (circled C and O in the counter map). Parallel with that the water $H_{11}$ is seen moving from $O_{10}$ to $O_3$, where there is a merging of valence basins between $H_{11}$ and $O_3$ signifies bond formation (surrounded by the small circle in the counter plot). The cycle comes to an end with $TS_V$, where the migrating $H_{14}$ is seen moving from $O_{12}$ to $C_5$, with 1.27 Å ($O_{12}$–$H_{14}$) and 1.47 Å ($H_{14}$–$C_5$) within a shared basin in the corresponding counter plot. ELF analysis for these transition states thus provides direct visual evidence of specific bond formations, cleavages, and electron reorganizations, lending strong support to the proposed mechanistic pathways and correlating well with the calculated energy barriers by highlighting the dynamic electronic events at each critical step.[54]

Additionally, non-covalent interactions (NCIs) using the Reduced Density Gradient (RDG) method[55] are represented in

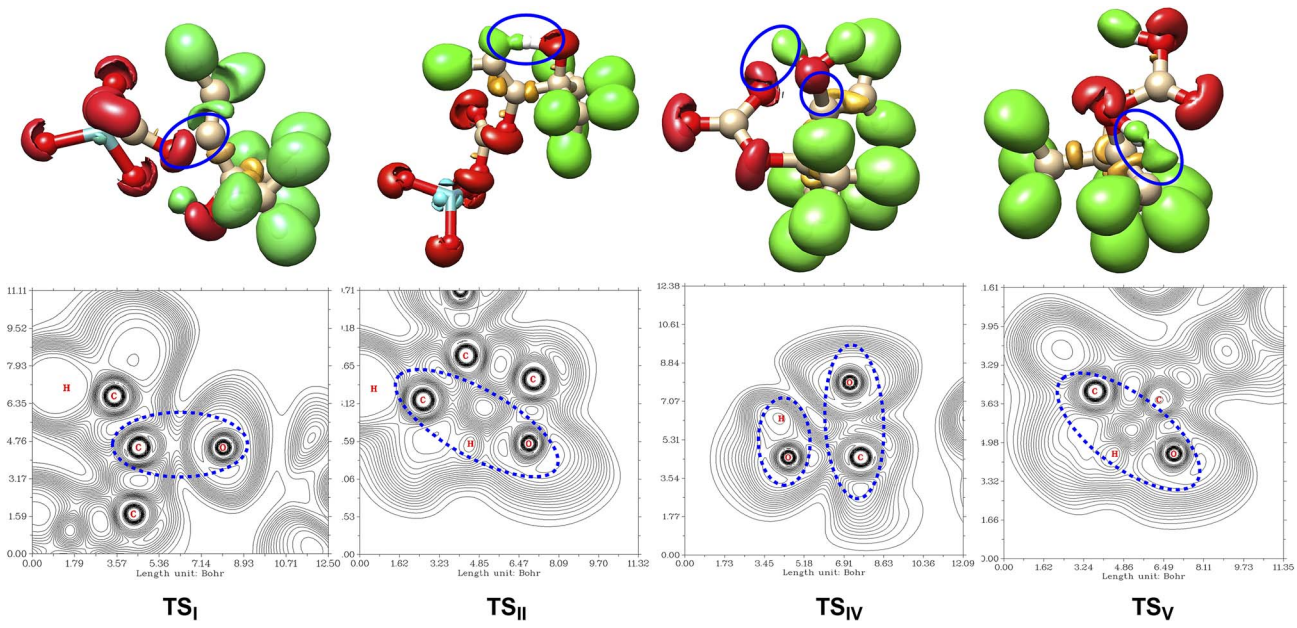


Fig. 7 Electron Localization Function (ELF) isosurfaces (top) and corresponding contour plots (bottom) illustrating electron density distributions at critical transition states for the oxomolybdate-catalyzed reaction. Blue circles emphasize regions of bond formation/breaking and electron reorganization.

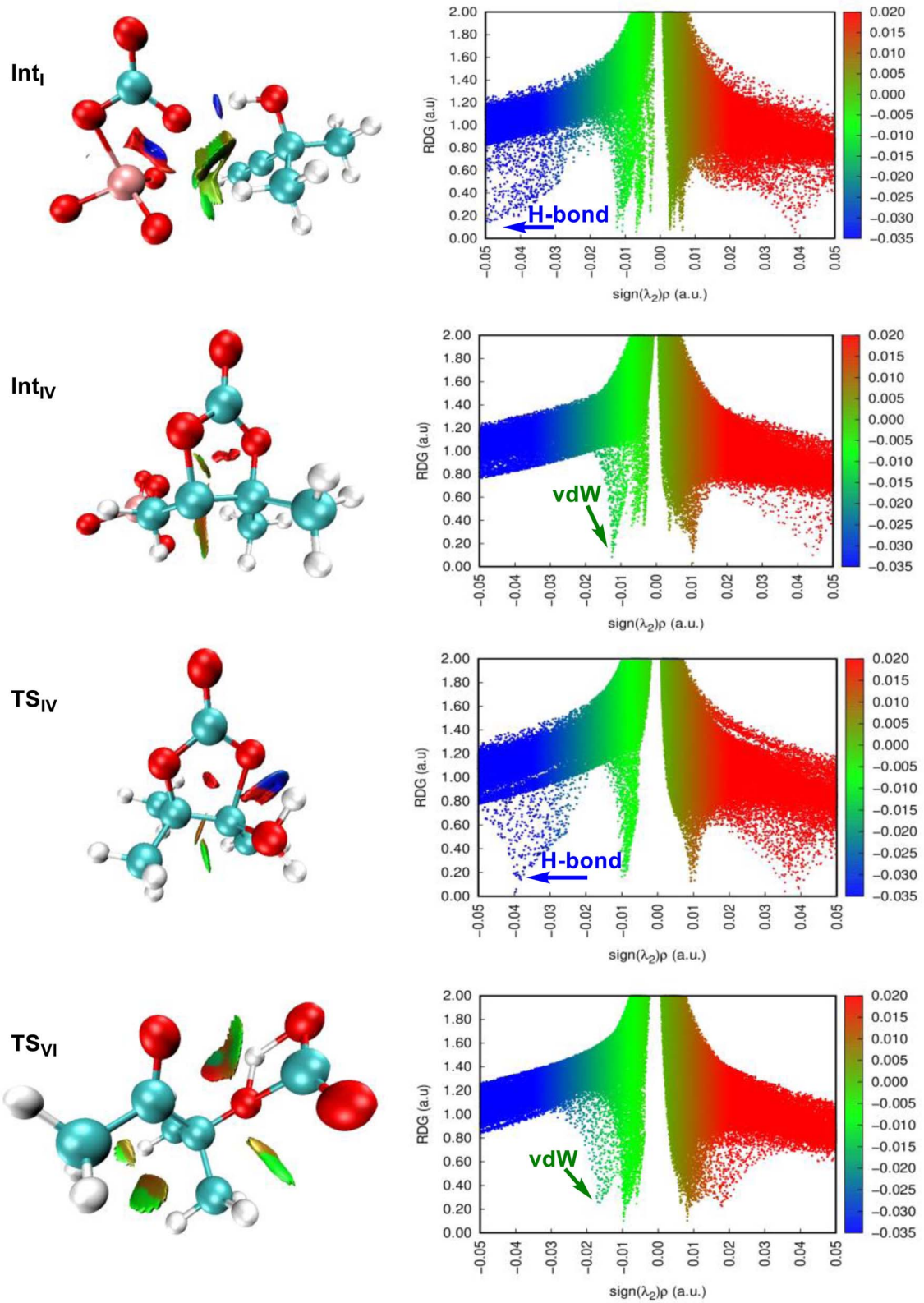


Fig. 8 NCI plots RDG isosurfaces (top row) and corresponding 2D scatter plots (bottom row) for key structures in the oxomolybdate catalyst reaction mechanism.

Fig. 8. The top panel displays 3D RDG isosurfaces, where the bottom 2D scatter plots of RDG *versus* sign ($\lambda_2$) $\rho$ distinguishes different quantitative types of NCIs based on the sign and magnitude of sign ($\lambda_2$) $\rho$ at low RDG values: blue indicates strong attractive interactions, green denotes weak attractive interactions, and red highlights strong repulsive interactions.

This qualitative and quantitative analysis of interactions is crucial for understanding the stability of intermediates and transition states in catalytic systems.[56,57] $Int_I$ represents the initial adduct of the oxomolybdate catalyst with the propargylic alcohol. RDG analysis indicates strong hydrogen-bonding interactions, visualized as prominent blue isosurfaces and reflected by a spike in the scatter plot at ($\mathrm{sign}(\lambda_2)\rho \approx -0.05$ a.u.). During the hydrolysis step (the rate-determining step, $TS_{IV}$), a strong attractive interaction crucial for ring opening emerges. Significant hydrogen bonds form between the water molecule and the carbonate oxygen, as indicated by low-density spikes around ($\mathrm{sign}(\lambda_2)\rho \approx -0.04$ a.u.). These interactions are further supported by hydrogen-bond lengths of 1.71 Å in $Int_I$ and 1.82 Å in $TS_{IV}$.

Moving to $Int_{IV}$, more extensive green areas are observed on the RDG isosurfaces, which suggests stronger van der Waals interactions ($\mathrm{sign}(\lambda_2)\rho = -0.01$ to 0.00 a.u.) indicates that weaker packing forces dominate the cyclized carbonate intermediate. Finally, the RDG analysis reveals the intrinsic non-covalent forces inside the stable molecular structure of the $CO_2$ elimination step ($TS_{VI}$). Green areas with the narrow range of ($-0.02 < \mathrm{sign}(\lambda_2)\rho < -0.01$ a.u.), signifying intramolecular van der Waals interactions that support the overall conformational stability of the ketone and the released $CO_2$.

## 4. Conclusion

The present work investigates the catalytic mechanisms of $CO_2$-promoted hydration of propargylic alcohols to α-hydroxy ketones mediated by oxometallate catalysts, $(MO_4\text{–}CO_2)^{2-}$ (M = Mo, Cr), using density functional theory (DFT). The main findings can be summarized as follows:

- A two-cycle catalytic pathway involving the active oxometallate–$CO_2$ adduct effectively describes the overall reaction mechanism.
- Quantum chemical descriptors reveal that nucleophilic activation of $CO_2$ by the oxometallate ionic liquids favors the molybdate species.
- Although both catalysts exhibit comparable overall energy barriers (29.9 and 29.8 kcal $mol^{-1}$), distinct turnover-determining intermediates (TDI) and turnover-determining transition states (TDTS) are observed.
- The oxomolybdate catalyst emerges as the more favorable system due to its higher chemical stability and lower toxicity compared to the oxochromate analogue.
- ELF and NCI analyses corroborate these findings, highlighting the decisive role of the metal center in governing key stabilization effects along the reaction pathway.

Overall, this study provides valuable mechanistic insights that can guide the rational design of efficient catalysts for $CO_2$-promoted chemical transformations.

## Conflicts of interest

The authors declare no conflicts of interest.

## Data availability

Supplementary information (SI): all data supporting this study, the fractional coordinates of all optimized structures. See DOI: https://doi.org/10.1039/d6ra00803h.

## Acknowledgements

The authors gratefully acknowledge the financial support provided by the Japan International Cooperation Agency (JICA) under Project No. TB1-25-07, which made this work possible. The authors also acknowledge the Centre for High Performance Computing (CHPC), South Africa, for providing the computational resources essential to this research.

## References

1 H. E. Ahmed, M. K. Albolkany, M. E. El-Khouly and A. Abd El-Moneim, *RSC Adv.*, 2024, **14**, 13946–13955.
2 K. R. Choi, Y.-J. Ahn and S. Y. Lee, *J. $CO_2$ Util.*, 2022, **58**, 101929.
3 D. Li, T. Lai, Y. Zhang, B. Han and G. Gao, *Mol. Catal.*, 2025, **575**, 114389.
4 Y. Zou, T. Leng, Y. Liu, W. Liu and W. He, *Org. Chem. Front.*, 2024, **11**, 6328–6333.
5 J. E. Hofferberth, H. Y. Lo and L. A. Paquette, *J. Org. Chem.*, 2021, **86**, 1311–1335.
6 M. Kutscheroff, *Ber. Dtsch. Chem. Ges.*, 1884, **17**, 13–29.
7 Y. Xing, M. Zhang, S. Ciccarelli, J. Lee and B. Catano, *Eur. J. Org Chem.*, 2017, 781–785.
8 A. Leyva and A. Corma, *J. Org. Chem.*, 2009, **74**, 2067–2074.
9 J. Santhi and B. Baire, *ChemistrySelect*, 2017, **2**, 4338–4342.
10 D. B. Grotjahn and D. A. Lev, *J. Am. Chem. Soc.*, 2004, **126**, 12232–12233.
11 S. Banerjee, S. B. Ambegave, R. D. Mule, B. Senthilkumar and N. T. Patil, *Org. Lett.*, 2020, **22**, 4792–4796.
12 Y. Zhang, J. Hu, Y. Xu, X. Yan, S. Zhang, K. Duan and F. Verpoort, *Appl. Catal., B*, 2022, **310**, 121270.
13 J. Li, G. Luo, Z. Liu and L. N. He, *J. $CO_2$ Util.*, 2021, **51**, 101625.
14 T. Fujinami, T. Suzuki, M. Kamiya, S.-i. Fukuzawa and S. Sakai, *Chem. Lett.*, 1985, **14**, 199–200.
15 X. Wang, Q. Dong, Z. Xu, Y. Wu, D. Gao, Y. Xu, C. Ye, Y. Wen, A. Liu and Z. Long, *Chem.–Eng. J.*, 2021, **403**, 126460.
16 J. Sun, Z. Li and J. Yin, *J. $CO_2$ Util.*, 2021, **53**, 101723.
17 N. M. Simon, M. Zanatta, F. P. Dos Santos, M. C. Corvo, E. J. Cabrita and J. Dupont, *ChemSusChem*, 2017, **10**, 4927–4933.
18 S. Dai, D. Jiang, X. Wang, H. Li, X. Luo and H. Luo, *Angew. Chem., Int. Ed.*, 2011, **50**, 7666–7669.
19 W. Deng, J. Yao, L. Shi, W. Wei, F. Chen and G. Xu, *Chem.–Eng. J.*, 2022, **427**, 131955.
20 X. Zhang, H. Dong, D. Bao, Y. Huang, X. Zhang and S. Zhang, *Ind. Eng. Chem. Res.*, 2014, **53**, 428–439.
21 D. D. Patel and J.-M. Lee, *Chem. Rec.*, 2012, **12**, 329–355.
22 H. Wang and B. Li, *Molecules*, 2024, **29**, 3216.

23 Y. Martinetto, B. Pegot, C. Roch-Marchal, B. Cottyn-Boitte and S. Floquet, *Eur. J. Inorg. Chem.*, 2020, 228–247.
24 X. Zhao, L. Guo, T. Xu, R. Zheng and H. Wang, *New J. Chem.*, 2022, **46**, 20092–20101.
25 W. Xu, J.-F. Cao, Y.-N. Lin, Y. Shu and J.-H. Wang, *Chem. Commun.*, 2021, **57**, 3367–3370.
26 Y. Wang, C. Wang, W. Lin, Q. Wang, B. Li, C. Chen, Y. Yuan and F. Verpoort, *Int. J. Mol. Sci.*, 2025, **26**, 1.
27 Y. Zhao and D. G. Truhlar, *Theor. Chem. Acc.*, 2008, **120**, 215–241.
28 S. Grimme, J. Antony, S. Ehrlich and H. Krieg, *J. Chem. Phys.*, 2010, **132**, 154104.
29 P. J. Hay and W. R. Wadt, *Chem. Phys.*, 1985, **82**, 270–283.
30 C. Lee, W. Yang and R. Parr, *Phys. Rev. B: Condens. Matter Mater. Phys.*, 1988, **37**, 785–789.
31 L. E. Roy, P. J. Hay and R. L. Martin, *J. Chem. Theory Comput.*, 2008, **4**, 1029–1031.
32 A. V. Marenich, C. J. Cramer and D. G. Truhlar, *J. Phys. Chem. B*, 2009, **113**, 6378–6396.
33 M. J. Frisch *et al.*, *Gaussian 16, Revision C.01*, Gaussian, Inc., Wallingford CT, 2016.
34 G. A. Zhurko, *Chemcraft: Graphical Program for Visualization of Quantum Chemistry Computations*, Ivanovo, Russia, 2005.
35 T. Lu and F. Chen, *J. Comput. Chem.*, 2012, **33**, 580–592.
36 E. D. Glendening, C. R. Landis and F. Weinhold, *J. Comput. Chem.*, 2019, **40**, 2234–2241.
37 E. D. Glendening and A. Streitwieser, *J. Chem. Phys.*, 1994, **100**, 2900–2909.
38 K. Mondal, A. K. Pal and P. K. Chattaraj, *J. Phys. Chem. C*, 2019, **123**, 12176–12182.
39 H. Wang, Y. Wu, B. Li and L. Zhang, *J. $CO_2$ Util.*, 2020, **40**, 101202.
40 R. G. Pearson, *J. Am. Chem. Soc.*, 1963, **85**, 3533–3539.
41 W. Yang and W. J. Mortier, *J. Am. Chem. Soc.*, 1986, **108**, 5708–5711.
42 R. G. Parr and W. Yang, *J. Am. Chem. Soc.*, 1984, **106**, 4049–4050.
43 S. Thabassum, V. Kumar, K. K. Gupta and M. Kumar, *J. Mol. Liq.*, 2024, **396**, 124016.
44 X. Zhang, Y. Liu and X. Li, *J. $CO_2$ Util.*, 2021, **48**, 101517.
45 L. Guo, X. Zhao and H. Wang, *Mol. Catal.*, 2020, **482**, 110695.
46 S. Kozuch and S. Shaik, *Acc. Chem. Res.*, 2011, **44**, 101–110.
47 G. S. Hammond, *J. Am. Chem. Soc.*, 1955, **77**, 334–338.
48 K. Kamiya, M. Boero, K. Shiraishi and A. Oshiyama, *J. Phys. Chem. B*, 2006, **110**, 4443–4450.
49 N. M. Wachter, E. H. Kreth and R. P. D'Amelia, *J. Chem. Educ.*, 2024, **101**, 2920–2924.
50 S. S. Wise and J. P. Wise, *Curr. Environ. Health Rep.*, 2019, **6**, 406–413.
51 J. A. Novotny and J. Evid, *Based Complementary Altern. Med.*, 2011, **16**, 164–168.
52 M. Weller, T. Overton, J. Rourke and F. Armstrong, *Inorganic Chemistry*, Oxford University Press, Oxford, 7th edn, 2018.
53 A. D. Becke and K. E. Edgecombe, *J. Chem. Phys.*, 1990, **92**, 5397–5403.
54 X. Zhang, D. Zhu, J. Chen, T. Liu, Y. Chen and Y. Liu, *Mol. Catal.*, 2024, **555**, 113886.
55 E. R. Johnson, S. Keinan, P. Mori-Sánchez, J. Contreras-García, A. J. Cohen and W. Yang, *J. Am. Chem. Soc.*, 2010, **132**, 6498–6506.
56 D. Sarma and A. K. Gupta, *Phys. Chem. Chem. Phys.*, 2024, **26**, 443–455.
57 M. M. El-Hendawy, I. M. Desoky and M. M. A. Mohamed, *Phys. Chem. Chem. Phys.*, 2021, **23**, 26919–26930.